OPEN ACCESS
IOP Publishing | IMMT
International Journal of Extreme Manufacturing
Int. J. Extrem. Manuf. 1 (2019) 032001 (12pp)
https://doi.org/10.1088/2631-7990/ab3b4e

Topical Review

At wavelength coherent scatterometry microscope using high-order harmonics for EUV mask inspection

Yutaka Nagata[1], Tetsuo Harada[2], Takeo Watanabe[2], Hiroo Kinoshita[2] and Katsumi Midorikawa[1,3]

[1] RIKEN Center for Advanced Photonics, RIKEN, 2-1 Hirosawa, Wako Saitama 351-0198, Japan
[2] Center for EUV Lithography, Laboratory of Advanced Science and Technology for Industry, University of Hyogo, Kamigori, Hyogo 678-1205, Japan

E-mail: kmidori@riken.jp

Received 31 July 2019
Accepted for publication 14 August 2019
Published 5 September 2019

Abstract

In this review, we describe our research on the development of the 13.5 nm coherent microscope using high-order harmonics for the mask inspection of extreme ultraviolet (EUV) lithography. EUV lithography is a game-changing piece of technology for high-volume manufacturing of commercial semiconductors. Many top manufacturers apply EUV technology for fabricating the most critical layers of 7 nm chips. Fabrication and inspection of defect-free masks, however, still remain critical issues in EUV technology. Thus, in our pursuit for a resolution, we have developed the coherent EUV scatterometry microscope (CSM) system with a synchrotron radiation (SR) source to establish the actinic metrology, along with inspection algorithms. The intensity and phase images of patterned EUV masks were reconstructed from diffraction patterns using ptychography algorithms. To expedite the practical application of the CSM, we have also developed a standalone CSM, based on high-order harmonic generation, as an alternative to the SR-CSM. Since the application of a coherent 13.5 nm harmonic enabled the production of a high contrast diffraction pattern, diffraction patterns of sub-100 ns size defects in a 2D periodic pattern mask could be observed. Reconstruction of intensity and phase images from diffraction patterns were also performed for a periodic line-and-space structure, an aperiodic angle edge structure, as well as a cross pattern in an EUV mask.

Keywords: high-order harmonics, coherent EUV light, EUV lithography, coherent EUV scatterometry microscope, synchrotron radiation, EUV mask inspection

(Some figures may appear in colour only in the online journal)

1. Introduction

Extreme ultraviolet (EUV) lithography with reflective photomasks is currently being refined for high-volume manufacturing (HVM) of chips with dimensions of 7 nm or less. ASML's NXE scanners are widely utilized by a multitude of semiconductor manufacturers. EUV scanners can replace the most critical (difficult multiple patterning) layers and provide lithography capabilities complementary to ArF technology.

[3] Author to whom any correspondence should be addressed.

2631-8644/19/032001+12$33.00

However, the fabrication and inspection of defect-free masks still remain one of the most critical issues facing EUV technology. Although defects on the mask have been reduced with each passing year, manufacturing defect-free EUV masks is still extremely difficult in practice. The development of inspection tools for EUV mask is paramount to detecting defects and thus producing defect-free EUV masks [1–4]. For the EUV mask blank inspection, Actinic blank inspection (ABI) tools [5, 6], based on darkfield microscopy, are widely used. This system satisfies the requirements for high-sensitivity and high-speed inspection of printable defects on mask blanks. Additionally, tools with a high magnification review mode improve defect position accuracy. As a result, information about EUV buried defects can be effectively obtained and analyzed with ABI tools. To mitigate mask defects, a pattern shift method has been developed to cover the multilayer defects under the absorber pattern. Because it is extremely difficult to prevent all defects, an EUV actinic review tool is essential for the inspection of printable phase defects on the patterned mask. However, there is no commercially available tool for the accurate determination of the precise shape of the buried defects on mask blanks or the printability of the defects in the patterned mask. Coherent scatterometry microscopy is one of the most attractive methods used to solve the aforementioned issues [7–11]. The coherent EUV scatterometry microscope (CSM) offers reflection mode coherent diffractive imaging (CDI) [12]. X-ray CDI [13–15] with synchrotron radiation (SR) has been widely used for biological and material applications. The CDI is a lensless system, where the image-forming optics are replaced by an inverse computation using scattered intensity. CDI is able to retrieve a phase in frequency space to reconstruct an aerial image.

We have developed the CSM system with a SR source to establish the actinic metrology as well as inspection algorithms [7–11]. We then demonstrated the reconstruction of the intensity and phase images of the line-and-space patterns (L/S), the cross pattern, and the programmed phase defect [9, 10]. A micro-CSM [16–19] that uses a Fresnel zone plate (FZP) to focus the coherent EUV light has also been constructed for the purpose of evaluating small phase defects on a mask blank. Observation of actual phase defects on a mask blank was then demonstrated using this system [12]. This information is crucial when pattern-shift is employed as a defect avoidance technique. However, because the SR is a large-scale facility and depletes most of the flux in obtaining coherent EUV light, it is not practical for real-world manufacturing applications.

High-order harmonics, however, is a promising alternative to SR for a table-top coherent EUV light source [20–23]. We have developed a phase-matched, high-order harmonics source for the CSM. In this study, we successfully generated low-divergence, coherent high-order harmonics in the EUV region with a commercial pumping laser [24]. Using the high-order harmonic generation (HHG)-CSM system, we observed programmed pattern defects in a periodic patterned mask. In the diffraction pattern from the EUV mask, a 2 nm wide line defect in an 88 nm line-and-space pattern as well as sub-100 ns sized absorber defects in a 112 nm hole pattern were both detected [25–27]. By further improving the system, we demonstrated the successful reconstructions of an-88 nm periodic L/S pattern and a cross-pattern with a quantitative phase contrast [28]. These results signify the that the standalone HHG-CSM system has tremendous potential.

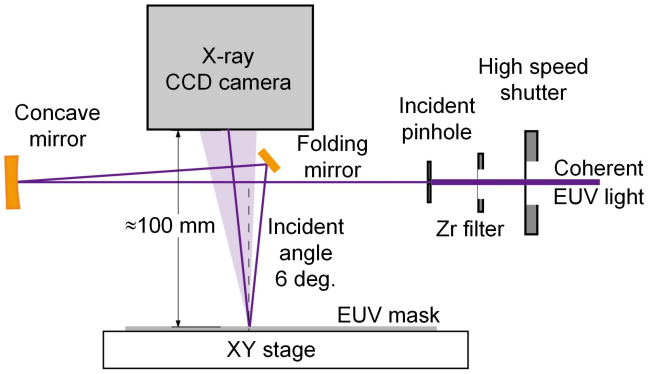

Figure 1. Schematic view of the CSM.

2. Key technologies of CSM system

2.1. CSM

A schematic view of the CSM is illustrated in figure 1. The CSM is composed of a concave mirror, a folding mirror, a piezo stage placed on the *XY* motor stage, an EUV filter, an EUV CCD camera, and a pinhole. These mirrors were coated with Mo/Si multilayer. A concave mirror placed on the linear stage is used to focus coherent EUV light onto the EUV masks. By using a folding mirror, the incident angle to the EUV mask is set at 6°, which is the same as that of current EUV lithography scanners. The EUV mask is placed on the stages to scan the observation points. The configuration is optimized for each coherent EUV light. The EUV mask is then exposed to a focused coherent EUV light. The diffraction patterns from the EUV mask are subsequently recorded by CCD camera. The surface of the CCD sensor is placed parallel to the mask surface. Two CCD cameras are exclusively used to alter the acceptance angle of the detector. The Roper Scientific MTE-2048B camera with 2048 × 2048, 13.5 μm size pixels is mainly employed as a detector. The EUV CCD camera is utilized because it can operate in a high-vacuum environment. The CCD camera is cooled to a temperature of −50 °C. Since the distance between the mask and CCD camera is about 100 mm, the spatial resolution is limited to 59 nm by numerical aperture (N.A.) of 0.14. As signal-to-noise ratio (SNR) is a key performance metric for the CSM, thus, we used the camera with 4 × 4 binning, where 4 × 4 pixels are treated as one pixel during readout. Therefore, the number of pixels with the binning condition was 512 × 512. The SNR has been thereby improved by a factor of 4.

2.2. CSM equipped with SR

The CSM was installed in the BL-3 beam line of the NewSUBARU synchrotron radiation facility, which employs

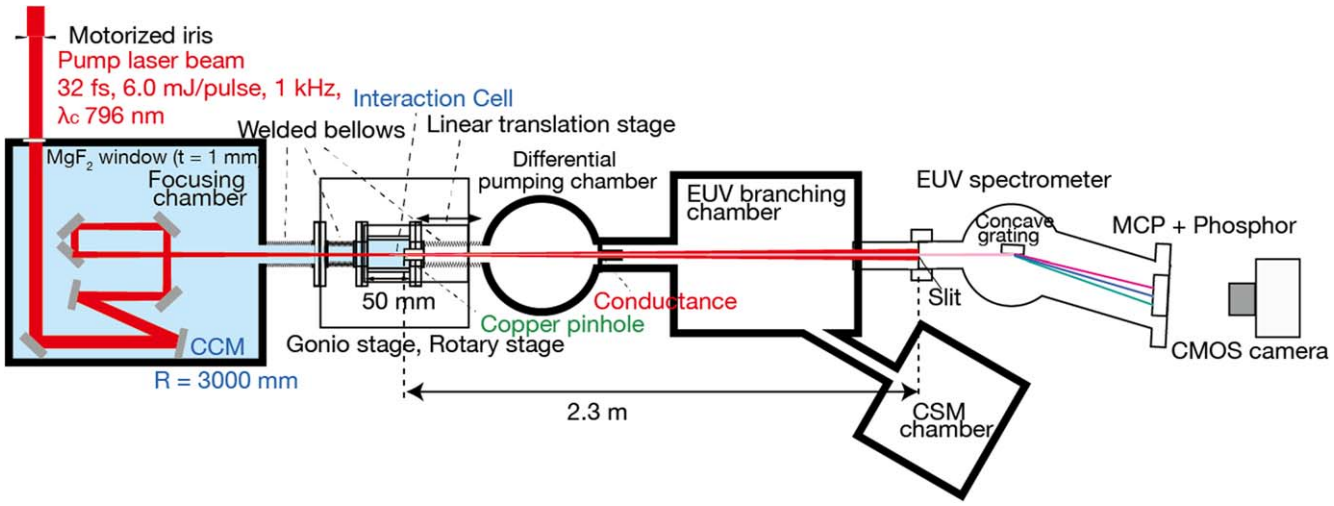

Figure 2. Experimental setup for high order harmonic generation.

a bending magnet as a light source [7, 8]. Two toroidal mirrors were used to collimate and deliver the SR to a concave mirror in the CSM system. Since the SR is partially coherent in time and space, a pinhole with a diameter of 5 μm was exposed to the SR to extract spatially coherent radiation. The pinhole is also used to stabilize the observation point on the EUV mask. The light that passed through the pinhole was focused onto the mask via a concave mirror with a curvature of 200 mm and a folding mirror at equal magnification. Those mirrors were coated with a Mo/Si multilayer and has a reflection bandwidth of 0.4 nm, which improves the temporal coherence. As a result of the spatial and temporal filtering, the coherent EUV power on the mask was reduced to 1.2 pW. The spatial coherence length of the incident beam is about 90 μm, as estimated from the divergence. This is substantially larger than the CSM-field size of 5 μm. The x–y stage can shift the EUV mask along the horizontal plane. The maximum travel range of the stage is $\pm$ 75 mm, for the full-field inspection of a 6″ EUV mask. The minimum step of the stage is 100 nm. Two encoders of Magnescale LASERSCALE were also monitored during the scan, the minimum step size of which is 34.5 nm.

2.3. HHG source

We have also developed a 13.5 nm HHG source equipped with a commercial Ti:sapphire laser (Spitfire pro 6 W) [24]. The laser delivers 1 kHz pulses with durations of 32 fs and energy up to 6.0 mJ, at a center wavelength of 796 nm. The laser beam diameter ($1/e^2$) was expanded from its original size of 9.5–12.0 mm by altering the configuration of the Galilean type beam expander, which was placed before the pulse compressor to reduce self-phase modulation. The laser system was installed on the Newport RS 2000 optical table. Figure 2 displays the experimental setup for HHG. A motorized iris diaphragm was placed in the pump laser path on the end of the optical table. The pump pulse was introduced through a 1 mm thick MgF_2 window into the focusing chamber and was loosely focused with an $R = 3000$ mm concave mirror. The angle of incidence on the concave mirror was optimized to correct the astigmatism of the pump pulse. The measured beam waist was about 90 μm in the vacuum. The maximum focused intensity in the vacuum was 1.1×10^{15} W cm^{-2}. Folding mirrors were then used to direct the pump pulse into the center of the entrance slit of an EUV spectrometer, which was also employed to adjust the focal point at the end of the interaction cell. The gas-filled region was sealed with a Cu foil at the end of the cell and subsequently evacuated with a dry pump into a vacuum of less than 10 Pa. A pinhole was drilled into the Cu foil by the attenuated pump pulses. The cell was mounted on a translation stage, which was combined with a gonio stage and a rotation stage. The position of the pinhole was then scanned axially along the beam. The differential pumping chamber, the branching chamber, and the EUV spectrometer were all evacuated with turbo molecular pumps. The spectrometer was maintained at a pressure below 10^{-5} Pa. The spectrometer, which was placed 2.3 m from the exit pinhole, is composed of a grazing incident flat-field grating and a microchannel plate assembly, coupled with a phosphor screen and a CMOS camera. In order to optimize the phase matching conditions for HHG, the target gas pressure should be adjusted to balance the geometrical phase shift as well as the dipole phase shift. The diameter of the iris alters not only the geometrical phase shift, but also the propagation of the intense pump laser pulse in the target gas. Therefore, the high-order harmonic output is extremely sensitive to the diameter of the iris. As a result of optimizing the phase matching conditions, the maximum pulse energy of the 59th harmonic was obtained in helium at a pressure of 15 kPa, during which the aperture diameter was set to 11.5 mm. The beam divergence of the harmonics was then measured to be 0.75 mrad. The spectral width of the 59th harmonic was also measured, resulting in a 0.09 nm full width at half-maximum, which approaches the resolution limit of the spectrometer.

Figure 3 demonstrates the pressure dependence of the high harmonic spectrum. At optimum pressure, the effective interaction intensity estimated from the cut-off wavelength [29] in the spectrum was 5×10^{14} W cm^{-2}. When the gas

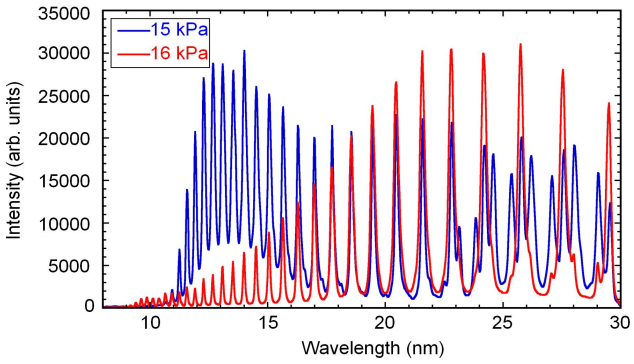

Figure 3. Observed high-harmonic spectra in helium.

pressure was increased from 15 to 16 kPa, the output of 59th harmonic decreased by a factor of 5. The results indicate that the phase matching conditions have been met, and the tunneling ionization does not affect phase matching conditions at this intensity [30]. This output energy was approximated from a photodiode (IRD SXUV-100) current, which was generated from two Zr filters. Since the current included not only the 59th harmonic output, but also harmonic outputs of other orders, the output energy was calibrated by taking the HHG output spectrum, photodiode quantum efficiency, and the filter spectrum into account as well. As a result, a high EUV output energy of 1 nJ/pulse (average power: 1 μW) was achieved [25].

2.4. Image reconstruction from diffraction patterns

The pattern images were reconstructed via ptychography [31–33], based on CDI algorithms. The sample is illuminated with step-and-repeat exposures. Diffraction images are then recorded at each step position. The step length should be shorter than the beam diameter such that an overlapped region is established. Hence, some diffraction images have overlapped sample information under different illumination conditions. The resulting redundancy in the data is essential in iterative reconstruction techniques. A sample aerial image is retrieved through iterative calculations of Fourier and inverse-Fourier transforms with constraints. In iterative calculations used in ptychography, the revised results of the reconstruction calculation are weighted by the probe amplitude. A nonuniform probe distribution is necessary for the image reconstruction process. Therefore, we used ptychographical coherent diffraction imaging in the CSM, which consists of a small probe and a large sample. Additionally, we also applied a modified phase-retrieval algorithm for ptychography, which simultaneously reconstructs the probe structure of the illuminating EUV light on the sample while the iteration is taking place. First, a complex amplitude distribution of an illumination probe was reconstructed using a prior pattern with a known shape and structure. A sample image was then reconstructed without the probe reconstruction algorithm. Lastly, the sample image was reconstructed with the probe reconstruction algorithm.

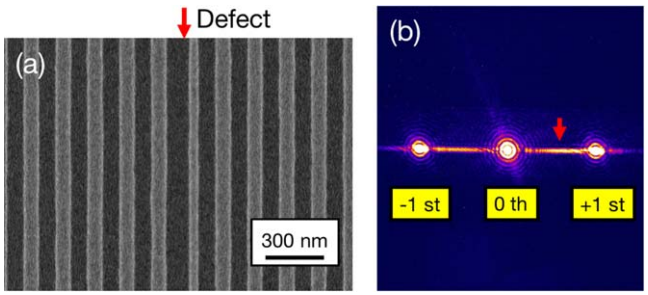

Figure 4. (a) SEM image and (b) diffraction pattern of a line-defect in 88 nm L/S pattern. Reproduced with permission from [9]. © 2011 American Vacuum Society.

3. SR-CSM system

We observed an amplitude defect in the absorber patterns using the SR-CSM system. Figure 4(a) displays the SEM image of the defect, which is a line defect in an 88 nm L/S pattern [9]. The defect line is 30 nm more narrow than the other lines. The defect linewidth varied from 2 to 40 nm, and the linewidth of the absorber ranged from 44 to 86 nm. Figure 4(b) shows the diffraction pattern resulting from the defect as well as the L/S patterns. The exposure time was 100 s. Diffraction from the defect was clearly captured as a line diffraction pattern in the transverse direction. As the defect linewidth was reduced, a broad diffraction pattern spread out on both sides of the 0th order maximum in the transverse direction. The defect signal signifying a defect size of up to 10 nm in width was detected in the diffraction pattern. Thus, the CSM is able to detect the defect as the difference within the observed diffraction pattern without the need to reconstruct the aerial image. This CSM inspection using the diffraction pattern also has the advantage of the ability to rapidly detect the existence of defects in the field of view. Nonetheless, image reconstruction is still essential for detecting the defect position. Theoretical detection limits for the defect sizes depend on the SNR of the detector noise, the source brightness, and the substrate roughness. The substrate roughness generates speckle noise onto the signal. If the detector noise is at an imaginary zero, then the detection limit is estimated to approximately 30 nm in the L/S patterned mask.

Figure 5(a) exhibits the image reconstruction result of the defect via ptychographical CDI. The defect was illuminated at 7 × 2 points with a 1 μm step [9]. A bright line results from the defect in the L/S pattern. However, the periodic L/S pattern around the defect produces a blurred shape due to the noise in the image reconstruction. We filtered out the diffraction from the periodic L/S signal and reconstructed the aerial image, as shown in figure 5(b). The defect was clearly detected without a periodic structure. Thus, the CSM can effectively inspect the defect positions through the application of ptychographical CDI.

Figure 6 displays a complex amplitude image with amplitude represented by brightness and phase represented by hue [10]. The sample pattern used was a crossed lines pattern with a width of 2 μm and a length of 10 μm, where the shape

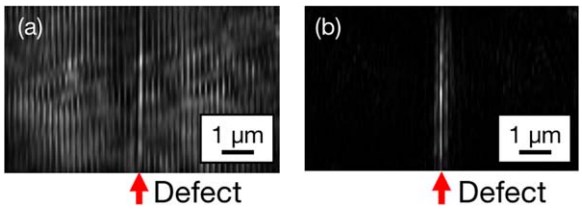

Figure 5. (a) Reconstruction image of line-defect and (b) that with the periodic signal filtered out. Reproduced with permission from [9]. © 2011 American Vacuum Society.

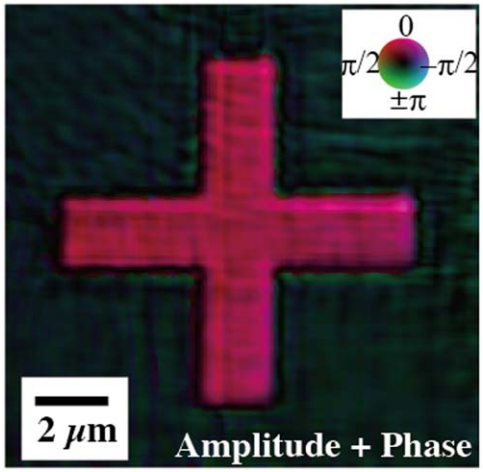

Figure 6. Complex amplitude image of crossed line pattern with the amplitude represented by brightness and the phase represented by hue. Reproduced from [10]. Copyright © 2013 The Japan Society of Applied Physics. All rights reserved.

was already known. Thirty-six diffraction patterns were used for the reconstruction. The sampling position was shifted in 2 μm steps, overlapping its 5 μm diameter with the probe. The cross shape was well-reconstructed with symmetrical results. As previously described, CDI retrieves the phase in frequency space to reconstruct the image. Therefore, the phase data of the aerial image in real space can be simultaneously reconstructed. The red region of the crossed line corresponds with the reflective multilayer region, and the dark green region corresponds with the absorber region. The phase difference between the absorber and reflection regions was found to be approximately 145°. The absorber region has a more advanced phase compared to the reflection region, similar to a bump structure, because the refractive index of the absorber is less than 1. The calculated phase shift is approximately 140°, comprising of an absorber structure with a 10 nm thick CrN buffer layer and a 51 nm thick Ta-based absorber, which is in line with the experimental values. The reflectivity of the absorber region was less than 2%, while that of the multilayer region was 62%. Although the reflectivity of the absorber was 31 times less than that of the reflection region, the absorber region information was not limited. The CSM records the interference of the reflection amplitude and found that the reflection amplitudes of the absorber and the multilayers were 0.14 and 0.79, respectively. For example, when the absorber to multilayer region ratio is 1:1 in the illumination probe field,

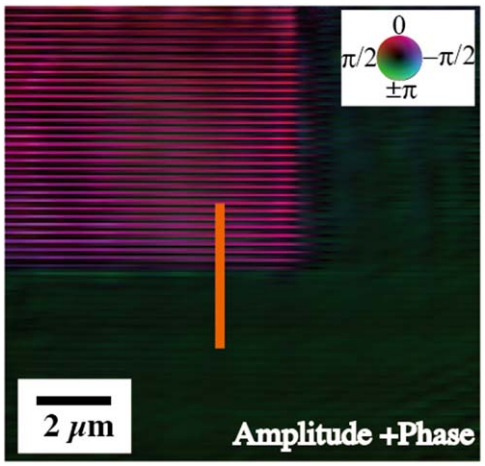

Figure 7. Complex amplitude images of a corner part of 88 nm L/S. The amplitude represented by brightness and the phase represented by hue pattern. Reproduced from [10]. Copyright © 2013 The Japan Society of Applied Physics. All rights reserved.

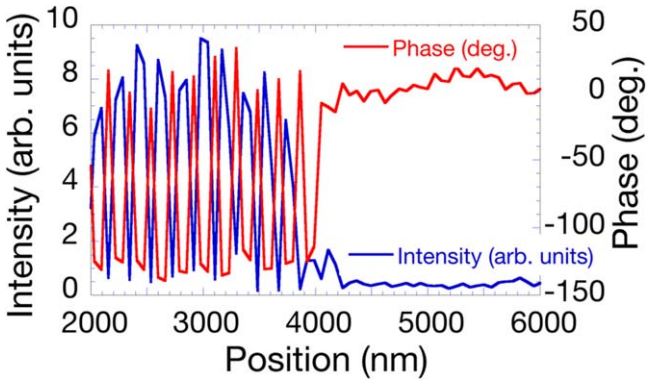

Figure 8. Profiles of intensity and phase at the position indicated by the orange line in figure 7. Adapted from [10]. Copyright © 2013 The Japan Society of Applied Physics. All rights reserved.

the contrast of the interference fringe is sufficiently high at 0.34. Thus, the CSM system is adept at providing the absorber region information.

Figure 7 presents the reconstructed complex amplitude images of a corner structure of an 88 nm L/S pattern, which is located on the same mask as the crossed line pattern [10]. 25 diffraction patterns were used for the reconstruction process. The position of the sample was shifted in 1.5 μm steps. The L/S structure and the corner structure were both successfully reconstructed. Figure 8 details the intensity and phase profiles at the position indicated by the orange line in figure 7. The phase difference between the absorber and the multilayer region is approximately 145°, which is identical to the reconstructed absorber phase shift shown in figure 8 [10]. This demonstrates that CSM can accurately and thoroughly evaluate the phase profile of the L/S pattern. These results clearly display that CSM is proficient at evaluating phase defects. When this system was put in practice, a programmed phase defect was evaluated successfully [10]. This technique has also been extended to a micro-CSM system and was once again successful in the evaluation of native phase defects.

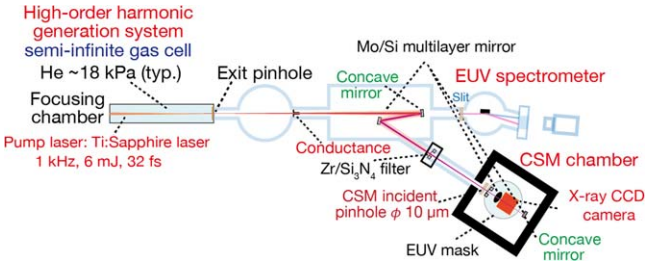

Figure 9. Optical double relay system for HHG-CSM system.

4. HHG-CSM system

4.1. Experimental setup

The configuration of the CSM is very similar to that of the SR-CSM system. Phase-matched high harmonics is used as a coherent EUV light. The beam divergence of the 59th harmonic was measured to be 0.75 mrad. Assuming that the harmonics is a Gaussian beam, the beam size at the exit pinhole is estimated to be 5.7 μm. The setup of the optical relay system is illustrated in figure 9 [25]. High harmonics is relayed onto an incident pinhole in the CSM chamber using a removable concave mirror with a radius of curvature of 2.0 m, as well as a flat mirror placed in the branching chamber. Those mirrors were coated with a Mo/Si multilayer which has a reflective bandwidth of approximately 0.4 nm near the wavelength of 13.5 nm. The 59th harmonic was selectively reflected and the magnification of the relay optics was 1.0. The Zr filter was placed between the branching chamber and the CSM chamber to remove the pump pulse, room light, and out-of-band radiation. The Zr filter is a free-standing membrane, with a 200 nm thick Zr layer and a 50 nm thick Si_3N_4 support layer. Since this tensioned filter has no wrinkles, the high spatial coherence will not be degraded. The 59th harmonic that passed through the pinhole was relayed onto the mask with a magnification of 1 $\times$ using both the concave mirror and the folding mirror (optical double relay system). The diameter of the incident pinhole is 10 μm which is approximately twice the minimum spot size of the 59th harmonic. The role of the pinhole is three-fold: (1) stabilization of observation point on the mask, (2) spatial filter to extract highly spatial coherent light from the 59th harmonic, and (3) spatial reduction filter for the pump pulse. Number 3 is crucial to the safe operation of the system. Since the intense pump pulse co-propagates with the harmonics, without a pinhole, if the Zr filter was accidentally damaged (such as by pump pulse, differential pressure, etc), the mask would be damaged by the pump pulse as well.

The large CCD image sensor is the most critical component of the CSM system used to directly record diffraction. The spatial resolution is dependent on the imaging area size of the CCD chip. Hence, a larger detector can record the diffraction pattern from a larger diffraction angle, which can provide higher-spatial-frequency information on the absorber pattern shape. In the HHG-CSM system, a CCD camera operate in a vacuum due to the optics layout, and the chip must be cooled down to -40 °C in order to reduce dark current noise. To achieve higher spatial resolution, we developed a state-of-the-art CCD camera with a large CCD image sensor (e2v technologies CCD230-84) of 61.4 $\times$ 61.4 mm^2 [25]. The number of pixels is 4096 $\times$ 4096 and the pixel size is 15 $\times$ 15 μm^2. The imaging area was then cooled down to a low temperature of -40 °C using a Peltier device. Accordingly, a low dark current noise of 0.02 electron/s/pixel was achieved. The NA is a function of sensor size and distance from the mask to the sensor, which is directly proportional to size and inversely proportional to distance. Since distance is restricted by both optics size and oversampling constraint, the camera recorded a high NA of 0.31 at the distance of 95 mm. The spatial resolution was thus enhanced to 27 nm.

4.2. Coherence evaluation of HHG

When the first experiment was conducted to analyze the spatial and temporal coherence of the harmonics, a 112 nm L/S pattern was used to generate high-order maxima in the sensor [25]. The coherent length of the harmonics is calculated to be 1.0 μm, while the maximum path difference at the sensor is calculated to be 3.0 μm. Although a full-field image was difficult to achieve with this setup, there were 10 other diffractions ($\pm$1st- to $\pm$5th-order diffractions) in addition to the 0th-order diffraction. Thus, the HHG EUV source demonstrated successful observation of the EUV mask. The new CCD camera recorded an extensive imaging area, including diffractions up to the 5th order. Figure 10(a) shows a diffraction pattern with a 2 nm wide line defect in an 88 nm L/S pattern, where the image contrast is adjusted to highlight the weak defect signal [25]. As indicated by the arrows, the line diffraction signal from the narrow line defect, which is not recorded in a defect-free region, is recorded here. The defect signal profile is illustrated in figure 10(c), the area of which is indicated by the red line. The signal profile displays the vertical signal distribution, where averaging in the horizontal direction is applied to reduce signal fluctuation. The defect signal is approximately 26 counts, where the background noise signal is approximately six counts. Therefore, the 2 nm wide defect is able to be clearly shown. Compared to previous results that used the SR light source, the HHG EUV source has a detection limit that is five times more narrow. Although the detection limit is influenced by multiple factors, the results evidently demonstrates that the spatial coherent of the 59th harmonic is high enough to observe defects on the nm-scale.

4.3. Beam pointing stabilization

The beam pointing stability is one of the most critical issues facing the HHG-CSM. Additionally, the beam size needs to be small enough to achieve high resolution in the CSM. In the aforementioned experiment, the diameter of the EUV light on the mask is approximately the same as that of the incident pinhole in the CSM chamber. Although the use of a small pinhole can reduce the beam size, it can also reduce the utilization efficiency of the EUV light. Furthermore, a beam

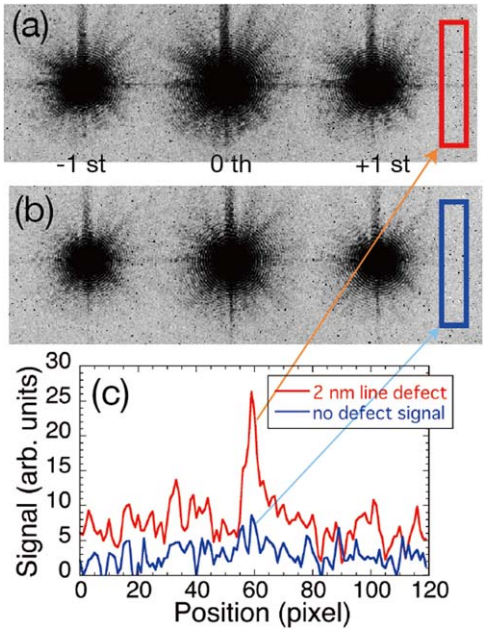

Figure 10. (a), (b) Observed diffraction patterns from an 88 nm L/S pattern, and (c) spatial profile of defect signal. Reproduced from [25]. Copyright © 2012 The Japan Society of Applied Physics. All rights reserved.

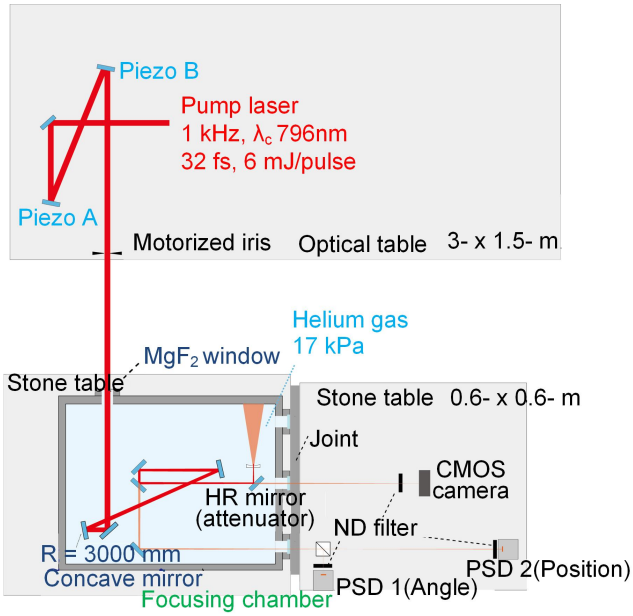

Figure 11. Schematic of the experimental setup for beam stabilization.

fluctuation larger than that of the incident pinhole diameter size is detrimental to the effective application of high harmonic light. When the EUV light at the exit pinhole is directly relayed with the concave mirror in the CSM chamber, the EUV light is de-magnified by a factor of less than 1/10. In this case, the beam-pointing fluctuations should be smaller than the beam size. The beam fluctuations of the pump beam was measured for a duration of 20 min at the focus, at ±23 μm (6.7 μm rms) and ±24 μm (7.2 μm rms) in the horizontal and vertical directions respectively. Relay optics would further increase beam fluctuations. Therefore, we installed a commercial product called 'Aligna: Automated Laser Beam Alignment and Stabilization System' in the HHG source.

The experimental setup is shown in figure 11 [27]. The system is composed of feedback control electronics, a combined angle and position detector (PSD), and two piezo-driven mirrors. A beam transmitted through a dielectric mirror was used as a reference beam for the beam stabilizer. A turning mirror then directs the beam to the PSD 2. A variable attenuator and a beam splitter, which direct the beam to the PSD 1, are both placed in the optical path. The PSD 1 is positioned at the focal point of the reference beam. The distance between the BS to the PSD 2 is approximately 40 cm. The power of the reference beam is at least 10 times stronger than the upper limit of the operation power of the PSD. During this experiment, the interaction cell was removed from the focusing chamber and a viewport flange was mounted on the exit port of the pump pulse. A CMOS camera was positioned at the focus to monitor the fluctuation of the pump pulse. The focusing chamber was subsequently filled with helium gas at a pressure of 17 kPa. The pump pulse was then attenuated before the viewport with a dielectric multilayer mirror. Figure 12 displays the *X*–*Y* plots of the beam positions observed over a

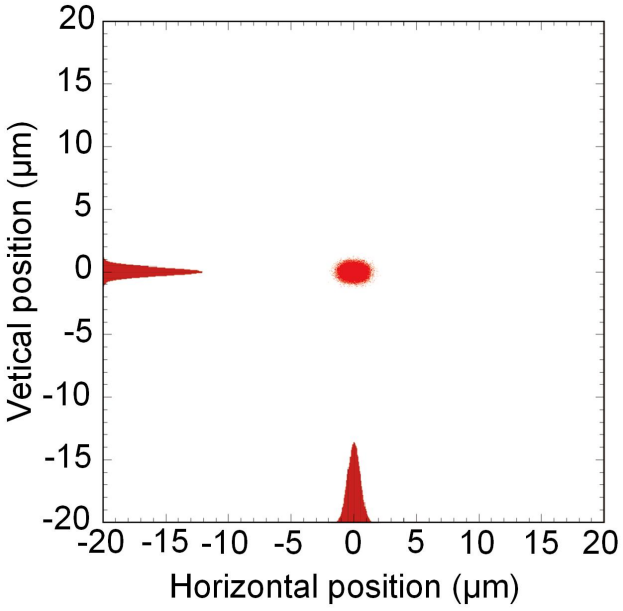

Figure 12. *X*–*Y* plots and histogram of the beam position of pump pulse observed at focus.

1 h period at the CMOS camera. The plots show that the fluctuation of the pump beam position has been markedly reduced to 0.3 μm rms (vertical) and 0.5 μm rms (horizontal).

4.4. Upgrade of optical relay system

The beam pointing fluctuation of the pump pulse was reduced to much less than that of the 59th harmonic beam size. Since the removal of the incident pinholes was made possible in the CSM chamber, we were able to enhance the relay optics to a

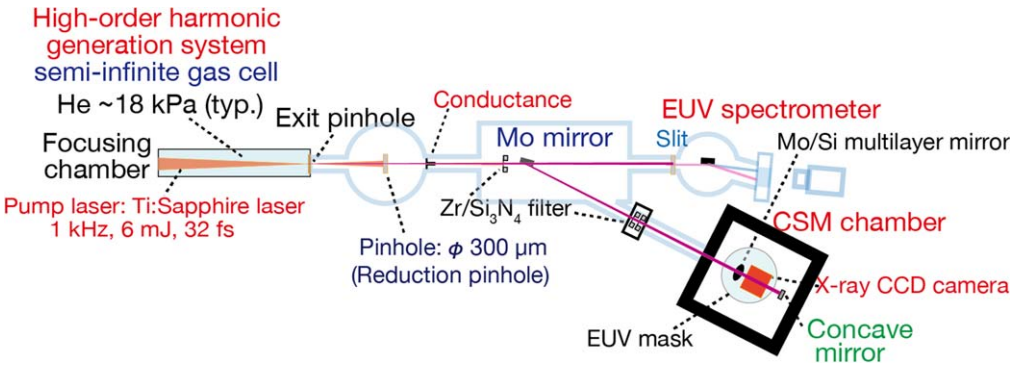

Figure 13. Upgraded optical relay for the HHG-CSM system.

single optical relay that can directly transfer the 59th harmonic beam to a mask. Instead of the incident pinhole, a reduction pinhole with a diameter of 300 μm was positioned inside the differential chamber for the purpose of spatial filtering the pump pulse and extracting the highly coherent EUV light [27]. The power of pump pulse was reduced by a factor of 100 by the pinhole. The transmitted EUV light was then directed to a concave mirror in the CSM chamber with a mirror coated with molybdenum thin-film. The angle of incidence on the mirror was 75°. The pump pulse power was further reduced by a factor of 10 after reflecting off the mirror, since the mirror serves as a Brewster plate for the pump pulse [34, 35]. The curvature radius of the concave mirror in the CSM chamber is approximately 350 mm. The distance from the EUV source to the focusing mirror and from the focusing mirror to the mask were 3.1 m and 185 mm, respectively. The magnification of the relay optics was approximately 1/17. Consequently, the utilization efficiency of the EUV light on the mask was improved 130 fold via beam pointing stabilization. The experimental setup is illustrated in figure 13.

4.5. Observation of diffraction pattern of programmed (absorber) defect

When a 2D periodic hole pattern mask is exposed to a coherent EUV light under the assumption that the beam diameter is much larger than the period of the pattern, intense interference maxima is expected appear in the diffraction pattern. In other words, in any location besides the interference maxima, the interference is almost destructive. Alternatively, if there exists a defect in the exposure area, a diffraction pattern would also be generated. In the destructive interference area, the diffraction pattern originated from the appearance of the defect. When such a diffraction pattern is observed, the shape of the defect can be approximated. In this experiment, a peak intensity ratio of two diffraction patterns resulting from a periodic pattern and a defect was considerably wider than the dynamic range of the CCD camera. To enable the observation of a defect's diffraction pattern, the defect signal needs to be higher than both the total integrated noise and the total diffraction pattern originated from the incoherent portion of the EUV light. Under such conditions, the resulting interference maximum was much higher than the saturation level of the sensor, while blooming and smear effects also appeared in the diffraction pattern. A 0.8 mm diameter pinhole was installed between the folding mirror and the EUV mask in order to reduce scattering from the optical element [27]. The focused beam radius ($1/e^2$ radius) on the mask was measured to be 3.9 μm, using knife edge method. We observed the EUV mask with hole patterns, which was fabricated in a square region measuring 25 $\times$ 25 μm^2, using a programmed absorber defect in the center. A 10 $\times$ 21 region of the hole in a block contained 10 defect shapes and 21 defect sizes. The block was surrounded with an absorber line that is 10 μm wide. We observed two hole blocks (112 and 180 nm in diameter), where both had a 1:1 ratio of hole to space width. Since the magnification of the exposure tool for EUV lithography is 1:4, the hole diameters correspond to 28 and 45 nm, respectively, on a wafer plane.

Figure 14(a) shows the difference image resulting from two diffraction patterns developed from defective (with 40 nm oversize defect) and defect-free areas in the 180 nm hole pattern [27]. The Gaussian blur filter is used to smooth the image, where the exposure time was 1 s. Figure 14(b) display a scanning electron microscopy (SEM) image of the defective area and corresponding defect shape, which are represented by the solid-orange region. As presented in figure 14(b), the shape of the hole and oversized defect is closer to that of a rounded square than a circle. The defect shape is the same as that of the region bounded by two concentric rounded squares. In the SEM image, a fringe pattern appears around the central maximum in both vertical and horizontal directions. The 1st and 2nd dark fringes are clearly observed. The distance between the dark fringes and intensity ratio of the 0th, 1st, 2nd fringes are accurately replicated by the calculation results. When double-relay optics was employed to detect the same defect, the required exposure time was 1000 s. This system reduced the exposure time dramatically to only 1 s. Figure 15(a) exhibits the SEM image of the defective area in the 180 nm hole pattern, as well as the difference image resulting from the two diffraction patterns produced by the defective and defect-free areas, respectively [27]. The solid-green region in figure 15 (a) represents the shape of the defect (no-hole defect). The diffraction pattern from no-hole defect is illustrated in figure 15(b). This pattern is identical to the diffraction pattern from a single hole. Since the intensity distribution of the interference fringes become close to that of the Airy-disc, the intensity of the 1st bright fringe is less than

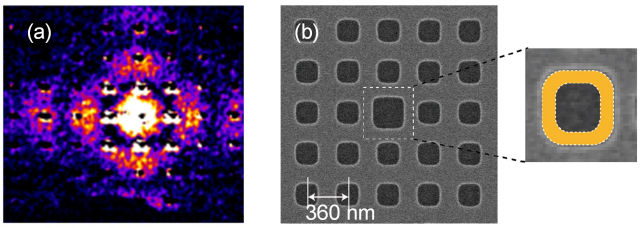

Figure 14. (a) Diffraction pattern and (b) SEM image.

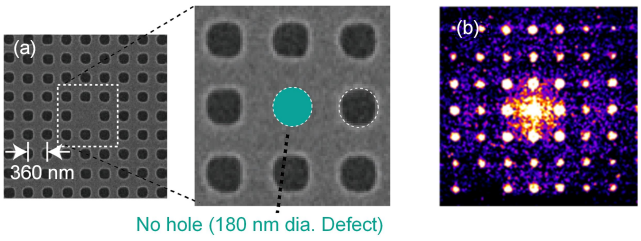

Figure 15. (a) SEM image and (b) diffraction pattern of no hole defect in 180 nm hole pattern.

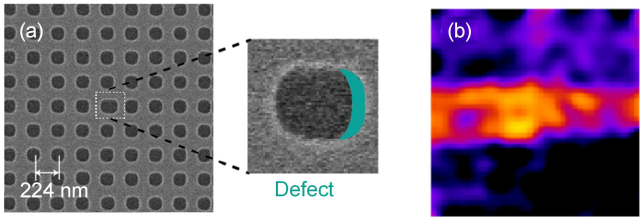

Figure 16. (a) SEM image and (b) diffraction pattern from line-end oversize defect in 112 nm hole pattern.

1/20 of that of the central bright fringe. Thus, the 1st dark fringe is barely noticeable, and the hole diameter calculated from the diameter of the 1st dark fringe is 200 nm.

Figure 16 reveals the SEM images of the line-end 24 nm oversized defect as well as the diffraction pattern resulting from the line-end 24 nm oversized defect in the 112 nm hole pattern, respectively [27]. This image is obtained using the following procedures (batch processing): (1) prior to the creation of a difference image, a Gaussian blur filter is applied to each diffraction pattern with a radius of 1 pixel. This processing is crucial to the reduction of camera noise in a difference image. When this processing is applied to the dark frame of the camera, a total noise count in the difference images of each dark frame is reduced by a factor of 3; (2) outliers are removed from the difference images and replaced by the mean value of the periphery areas; and (3) the Gaussian blur filter is applied to smooth out the image. In the diffraction pattern resulting from a line-end 24 nm oversized defect, an averaged signal (count) is only three. Nonetheless, the shape of the diffraction pattern is accurately replicated by the calculation. The result suggests that the incoherent portion of the EUV light does not affect the observation of small signals. We observed these defects using the line step-and-scan method. A defect can be detected with 1 μm steps in a single direction, scanning from one edge to the other of a hole

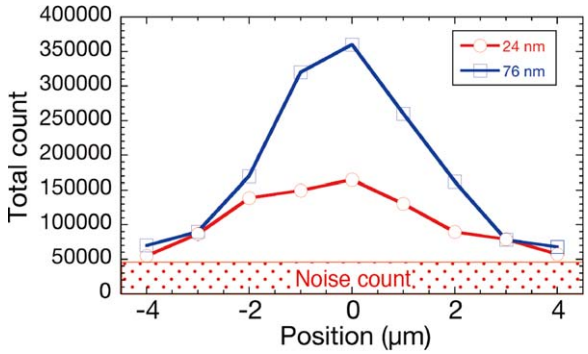

Figure 17. Total count of the defect signal from extended defect via step-scan measurements.

region (25 μm length). The fluctuation of the diffraction signal intensity is 1.8% (1σ) over 10 min.

Figure 17 illustrates the relationship between the position of the defect and the integrated total count of the defect signal resulting from 24 and 76 nm line end oversized defects. The total count of defect signals is calculated via the aforementioned batch processing method. The background noise consists of the CCD camera and EUV mask noise. The CCD camera noises are results from dark current and readout noises. EUV mask noises are induced by the roughness of the multilayer and the absorber. The integrated defect signal for each defect shape is almost proportional to the defect area size and the illumination power. In this study, the shape of the defects can be deduced from the diffraction pattern without reconstruction of the image. Specifically, when the interference fringe appears, a more detailed shape can be approximated. Obviously, the diffraction pattern does not include the position information of the defect, though the approximate position can be determined by a step-scan measurement. A diffraction pattern be generated not only from a pattern defect but also from a phase defect. If a phase defect exists under the hole pattern, the diffraction pattern of the phase defect can be identified. The detection limit is a line-end 24 nm oversized defect with a 10 s exposure time, which has an area of 2688 nm^2. This area is equivalent to that of a 52 $\times$ 52 nm^2 absorber defect. These results indicate that the spatial coherence of the 59th harmonic is high enough to observe such a small signal within a high contrast signal. The detection limit of the defect size is roughly proportional to the illumination size. Thus, reduction of the illumination size will dramatically improve the detection limit. However, reconstruction of complex images is required to obtain detailed characteristics of the defect.

4.6. Reconstruction of absorber patterns from diffraction patterns

In order to reconstruct the EUV mask pattern through ptychography, diffraction images were obtained via step-and-repeat measurement. Ultra-precise sample stage positioning is required to reconstruct the images. Similarly, the beam pointing and beam profile needs to be stable. In the above experiment, the reduction pinhole was fabricated with a

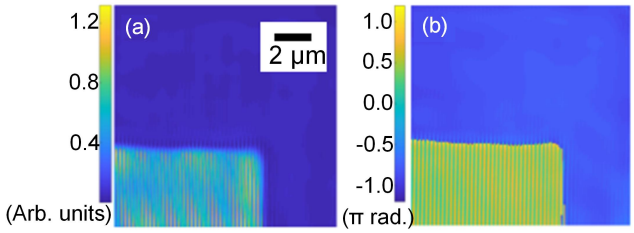

Figure 18. Reconstructed results of the corner structure of the 88 nm L/S pattern in terms of (a) intensity and (b) phase. Adapted from [28]. Copyright © 2017 The Japan Society of Applied Physics. All rights reserved.

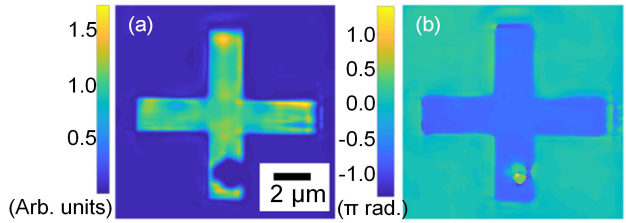

Figure 19. Reconstructed results of the cross-line pattern in terms of (a) intensity and (b) phase contrast. Native defect on the cross-line is also reconstructed. Adapted from [28]. Copyright © 2017 The Japan Society of Applied Physics. All rights reserved.

SUS304 steel plate of 1 mm thickness [28]. However, the pinhole was deformed due to heat produced by the high-power pump laser beam. The deformation of the pinhole thus affected the beam quality of the 59th harmonic. Therefore, reconstructing the EUV mask pattern was challenging. To improve the stability of the EUV light spatial profile, a tungsten pinhole with high thermal resistance was used. The thickness of this tungsten pinhole was the same as that of the SUS304 pinhole (1 mm). The melting point of tungsten is 3,420 °C, which is 2.4 times higher than that of SUS304 (1400 °C). Thus, the $1/e^2$ spot radius of the focused EUV light, measured using the knife edge scan method, was reduced to 1.6 μm.

For high-precision sample positioning, a piezo flexure xy stage (Piezosystem Jena PXY 200SG) was installed onto the pulse motor stage, which had an integrated strain gauge for position feedback. The stroke length is 160 μm in the x- and y-directions. The resolution is 4 nm and the repeatability is 45 nm. The accuracy of the mask stage position for ptychography was significantly improved with this setup. To establish an accurate comparison, this experiment used the same sample as before. Two types of absorber patterns were observed. One is an 88 nm L/S pattern, designed in a square region with an area of 25 × 25 μm^2. Its line-to-space ratio is 1–1. The other is a cross line-pattern with a width of 2 μm and length of 10 μm. Diffraction patterns from the cross-line pattern and the 88 nm L/S pattern were recorded by the CCD camera. The measurement was conducted at 15 × 15 points for step-and-repeat measurements. The exposure time was 0.3 s at each point and the readout time of the CCD camera was 4.5 s per image. The total observation time was 17 min at 15 × 15 points, where the readout time was dominant to the observation time. Since the spatial profile stability of the HHG EUV source was greatly improved by the tungsten reduction pinhole, diffractions from the pattern were clearly recorded. Figure 18 displays a reconstructed image of the corner structure of the 88 nm L/S pattern [28], where figure 18(a) shows the intensity image and figure 18(b) exhibits the phase image. As revealed in figure 18, the line and corner structures are well-reconstructed. Additionally, the phase image demonstrates that the phase modulation of the line pattern is clearly observed. Thus, the CSM can clearly and accurately observe the absorber pattern phase, which is critical in predicting the mask-induced aberration.

Figure 19 illustrates a reconstructed image of the cross-line pattern [28]. The intensity image is shown in figure 19(a) and the phase image in figure 19(b). The cross structure shown here is also well-reconstructed. The reconstructed image quality resulting from the HHG-CSM is higher than that resulting from the SR-CSM (figures 6 and 7) since both the EUV light power and position accuracy was significantly improved. Using the phase image, we were able to estimate the phase shift of the absorber pattern. The cross-line region is the reflective multilayer without the absorber. The outer region of the cross structure was covered by the absorber layer. The difference between the absorber and reflective regions was estimated to be 2.8 rad (160°). The CSM can estimate the absorber phase shift, which is essential to achieving the attenuated phase-shift mask [36–39]. In addition to the cross pattern, a natural defect that appears to be a particle of ~2 μm on the pattern was also observed. The phase shift of the particle was the same as that of the absorber pattern, which indicated that this particle is a peeled absorber. As shown, the phase shift is extremely advantageous for characterizing the defect origin. Hence, phase information is essential for achieving an accurate and thorough inspection of the mask.

5. Advanced HHG-CSM system

For the inspection of printable defects, the probe beam size should be less than ~100 nm. An FZP is a key optical element for focusing of high harmonics on the sub-μm scale. An off-axis short focal length zone plate can be integrated into an EUV mask scanning microscope equipped with an HHG source [40–42]. A lower divergence beam is required to increase the coupling efficiency between an EUV light and an FZP. With a lower divergence, a Gaussian profile harmonic emission with a divergence of 0.18 mrad ($1/e^2$) was obtained under another phase matching condition in helium. The beam divergence of the 59th harmonic is approximately 1/20 of that of the pump pulse. Thus, the majority of the low divergence beam can pass through the reduction pinhole. Compared to previous results, though the pulse energy of the 59th harmonic is about 1/3, the fluence of the harmonic is ~5 times higher. Therefore, the advantage of the low divergence beam is the ability to not only improve spatial coherence, but also the utilization efficiency of the HHG-CSM system harmonic.

Consequently, the illumination power on the mask is increased. The beam radius of 24 μm at the exit pinhole, estimated by the relationship between the beam waist and the divergence of Gaussian beam, is much larger than the pointing fluctuations of the pump pulse. The pointing stability of the EUV light on the mask will be further improved by applying the low divergence beam. Combining the lower divergence coherent high harmonic beam with FZP technologies will significantly improve the resolution limit of the HHG-CSM system.

6. Conclusion

We have developed a CSM system using a SR source to establish actinic metrology and inspection algorithms. The diffraction patterns of an 88 nm L/S pattern and crossed-like pattern with a width of 2 μm on the EUV mask were observed using the SR-CSM system. The complex images of the mask patterns were accurately reconstructed from the observed images through applying the modified phase retrieval algorithm. The results demonstrate that the SR-CSM system can evaluate absorber phase shift values qualitatively. For the practical application of the CSM, we also developed a standalone, coherent EUV light source based on high-order harmonic generation with a table-top, commercial Ti:sapphire laser. By installing the beam stabilization apparatus, the beam fluctuation of the pump pulse becomes much smaller than the radius of the 59th harmonic. Consequently, the utilization efficiency of the EUV light on the mask was drastically improved with the usage of upgraded relay optics. Even diffraction patterns of small defects (on nm-scale) can be observed. The results indicate that HHG-CSM inspection using the diffraction pattern can both efficiently and effectively detect the existence of defects in the field of view, as well as the fact that the 59th harmonic meets the spatial coherence requirement for the CSM. Furthermore, the reconstruction of the complex image of the mask pattern was also demonstrated using the 59th harmonic. The reconstructed image quality resulting from the HHG-CSM was higher than that resulting from the SR-CSM, due to the improvement of both position accuracy and EUV light power. Thus, the state-of-the-art HHG-CSM will undoubtedly be a powerful tool for EUV mask inspection in factories, such as mask shops and semiconductor fabrication plants, around the world.

ORCID iDs

Yutaka Nagata https://orcid.org/0000-0002-6356-2962

References

[1] Terasawa T, Yamane T, Tanaka T, Suga O and Tomie T 2010 Actinic phase defect detection for extreme ultraviolet lithography mask with absorber patterns *Japan. J. Appl. Phys.* **49** 06GD02

[2] Kwon H J, Harris-Jones J, Teki R, Cordes A, Nakajima T, Mochi I, Goldberg K A, Yamaguchi Y and Kinoshita H 2011 Printability of native blank defects and programmed defects and their stack structures *Proc. SPIE* **8166** 81660H

[3] Mochi I, Goldberg K A, La Fontaine B, Tchikoulaeva A and Holfeld C 2010 Actinic imaging of native and programmed defects on a full-field mask *Proc. SPIE* **7636** 76361A

[4] Mochi I, Goldberg K A, Xie R, Yan P-Y and Yamazoe K 2011 Quantitative evaluation of mask phase defects from through-focus EUV aerial images *Proc. SPIE* **7969** 79691X

[5] Tchikoulaeva A, Miyai H, Suzuki T, Takehisa K, Kusunose H, Yamane T, Terasawa T, Watanabe H, Inoue S and Mori I 2013 EUV actinic blank inspection: from prototype to production *Proc. SPIE* **8679** 86790I

[6] Suzuki T, Miyai H, Takehisa K, Kusunose H, Watanabe H and Mori I 2015 Detection capability of Actinic Blank Inspection tool *Proc. SPIE* **9658** 96580O

[7] Harada T, Nakasuji M, Tada M, Nagata Y, Watanabe T and Kinoshita H 2011 Critical dimension measurement of an extreme-ultraviolet mask utilizing coherent extreme-ultraviolet scatterometry microscope at NewSUBARU *Japan. J. Appl. Phys.* **50** 06GB03

[8] Harada T, Kishimoto J, Watanabe T and Kinoshita H 2009 Mask observation results using a coherent extreme ultraviolet scattering microscope at NewSUBARU *J. Vac. Sci. Technol.* B **27** 3203–7

[9] Harada T, Nakasuji M, Kimura T, Watanabe T and Kinoshita H 2011 Imaging of extreme-ultraviolet mask patterns using coherent extreme-ultraviolet scatterometry microscope based on coherent diffraction imaging *J. Vac. Sci. Technol.* B **29** 06F503

[10] Harada T, Nakasuji M, Nagata Y, Watanabe T and Kinoshita H 2013 Phase imaging of extreme-ultraviolet mask using coherent extreme-ultraviolet scatterometry microscope *Japan. J. Appl. Phys.* **52** 06GB02

[11] Harada T, Nakasuji M, Nagata Y, Watanabe T and Kinoshita H 2013 Phase imaging of EUV masks using a lensless EUV microscope *Proc. SPIE* **8701** 870119

[12] Seaberg M D, Zhang B, Gardner D F, Shanblatt E R, Murnane M M, Kapteyn H C and Adams D E 2014 Tabletop nanometer extreme ultraviolet imaging in an extended reflection mode using coherent Fresnel ptychography *Optica* **1** 39–44

[13] Miao J, Sayre D and Chapman H N 1998 Phase retrieval from the magnitude of the Fourier transforms of nonperiodic objects *J. Opt. Soc. Am.* A **15** 1662–9

[14] Miao J, Charalambous P, Kirz J and Sayre D 1999 Extending the methodology of x-ray crystallography to allow imaging of micrometre-sized non-crystalline specimens *Nature* **400** 342–4

[15] Miao J, Ishikawa T, Anderson E H and Hodgson K O 2003 Phase retrieval of diffraction patterns from noncrystalline samples using the oversampling method *Phys. Rev.* B **67** 174104

[16] Harada T, Tanaka Y, Watanabe T and Kinoshita H 2013 Phase defect characterization on an extreme-ultraviolet blank mask using microcoherent extreme-ultraviolet scatterometry microscope *J. Vac. Sci. Technol.* B **31** 06F605

[17] Tanaka Y, Harada T, Amano T, Usui Y, Watanabe T and Kinoshita H 2014 Characterization of small phase defects using a micro-coherent extreme ultraviolet scatterometry microscope *Japan. J. Appl. Phys.* **53** 06JC03

[18] Harada T, Hashimoto H, Tanaka Y, Amano T, Watanabe T and Kinoshita H 2015 Quantitative phase imaging of a small phase structure on an extreme-ultraviolet mask by coherent diffraction imaging *Appl. Phys. Express* **8** 055202

[19] Harada T, Hashimoto H, Amano T, Kinoshita H and Watanabe T 2016 Actual defect observation results of an

extreme-ultraviolet blank mask by coherent diffraction imaging *App. Phys. Express* **9** 035202

[20] Tamaki Y, Itatani J, Nagata Y, Obara M and Midorikawa K 1999 Highly efficient, phase-matched high-harmonic generation by a self-guided laser beam *Phys. Rev. Lett.* **82** 1422–5

[21] Zhang X *et al* 2004 Highly coherent light at 13 nm generated by use of quasi-phase-matched high-harmonic generation *Opt. Lett.* **29** 1357–9

[22] Takahashi E J, Nabekawa Y and Midorikawa K 2004 Low-divergence coherent soft x-ray source at 13 nm by high-order harmonics *Appl. Phys. Lett.* **84** 4–7

[23] Painter J C, Adams M, Brimhall N, Christensen E, Giraud G, Powers N, Turner M, Ware M and Peatross J 2006 Direct observation of laser filamentation in high-order harmonic generation *Opt. Lett.* **31** 3471–4

[24] Nagata Y, Harada T, Nakasuji M, Kinoshita H and Midorikawa K 2013 Development of coherent EUV scatterometry microscope with high-order harmonic for EUV mask inspection *Proc. SPIE* **8849** 884914

[25] Nakasuji M, Tokimasa A, Harada T, Nagata Y, Watanabe T, Midorikawa K and Kinoshita H 2012 Development of coherent extreme-ultraviolet scatterometry microscope with high-order harmonic generation source for extreme-ultraviolet mask inspection and metrology *Japan. J. Appl. Phys.* **51** 06FB09

[26] Kinoshita H, Harada T, Nagata Y, Watanabe T and Midorikawa K 2014 Development of EUV mask inspection system using high-order harmonic generation with a femtosecond laser *Japan. J. Appl. Phys.* **53** 086701

[27] Fujino T, Tanaka Y, Harada T, Nagata Y, Watanabe T and Kinoshita H 2015 Extreme ultraviolet mask observations using a coherent extreme ultraviolet scatterometry microscope with a high-harmonic-generation source *Japan. J. Appl. Phys.* **54** 06FC01

[28] Mamezaki D, Harada T, Nagata Y and Watanabe T 2017 Imaging performance improvement of coherent extreme-ultraviolet scatterometry microscope with high-harmonic-generation extreme-ultraviolet source *Japan. J. Appl. Phys.* **56** 06GB01

[29] Corkum P B 1993 Plasma perspective on strong field multiphoton ionization *Phys. Rev. Lett.* **71** 1994–7

[30] Constant E, Garzella D, Breger P, Mével E, Dorrer C, Le Blanc C, Salin F and Agostini P 1999 Optimizing high harmonic generation in absorbing gases: model and experiment *Phys. Rev. Lett.* **82** 1668–71

[31] Rodenburg J M and Faulkner H M L 2004 A phase retrieval algorithm for shifting illumination *Appl. Phys. Lett.* **85** 4795–7

[32] Thibault P, Dierolf M, Menzel A, Bunk O, David C and Pfeiffer F 2008 High-resolution scanning x-ray diffraction microscopy *Science* **321** 379–82

[33] Humphry M J, Kraus B, Hurst A C, Maiden A M and Rodenburg J M 2012 Ptychographic electron microscopy using high-angle dark-field scattering for sub-nanometer resolution imaging *Nat. Commun.* **3** 730

[34] Takahashi E J, Hasegawa H, Nabekawa Y and Midorikawa K 2004 High-throughput, high-damage-threshold broadband beam splitter for high-order harmonics in the extreme-ultraviolet region *Opt. Lett.* **29** 507–9

[35] Nagata Y, Furusawa K, Nabekawa Y and Midorikawa K 2007 Single-shot spatial-coherence measurement of 13 nm high-order harmonic beam by a Young's double-slit measurement *Opt. Lett.* **32** 722–4

[36] Yan P-Y, Myers A, Shroff Y, Chandhok M, Zhang G, Gullikson E and Salmassi F 2011 EUVL alternating phase shift mask *Proc. SPIE* **7969** 79690G

[37] Kamo T, Aoyama H, Tanaka T and Suga O 2007 Impact of mask absorber properties on printability in EUV lithography *Proc. SPIE* **6730** 673017

[38] Tanabe H, Murachi T, Lee S H, Chandhok M, Park S-J, Zhang G, Abe T, Ogase T and Hayashi N 2011 Phase-shifting effect of thin-absorber EUV masks *Proc. SPIE* **8166** 816618

[39] Murachi T, Tanabe H, Park S-J, Gullikson E, Ogase T, Abe T and Hayashi N 2012 Direct phase-shift measurement of thin and thick absorber EUV masks *Proc. SPIE* **8441** 84411M

[40] Pan H, Späth C, Guggenmos A, Chew S H, Schmidt J, Zhao Q-Z and Kleineberg U 2016 Low chromatic Fresnel lens for broadband attosecond XUV pulse applications *Opt. Express* **24** 16788–98

[41] Mochi I, Helfenstein P, Mohacsi I, Rajendran R, Yoshitake S and Ekinci Y 2017 RESCAN: an actinic lensless microscope for defect inspection of EUV reticles *Proc. SPIE* **10143** 101431O

[42] Naulleau P P *et al* 2014 Electro-optical system for scanning microscopy of extreme ultraviolet masks with a high harmonic generation source *Opt. Express* **22** 20144–54